

RESEARCH

Open Access



Abrogation of ORF8–IRF3 binding interface with Carbon nanotube derivatives to rescue the host immune system against SARS-CoV-2 by using molecular screening and simulation approaches

Muhammad Suleman^{1,2†}, Abduh Murshed³, Kashif Imran⁴, Abbas Khan^{5,6†}, Zafar Ali², Norah A. Albekairi⁷, Dong-Qing Wei⁵, Hadi M. Yassine^{8,9*} and Sergio Crovella^{1*}

Abstract

The COVID-19 pandemic, caused by the SARS-CoV-2 virus, has led to over six million deaths worldwide. In human immune system, the type 1 interferon (IFN) pathway plays a crucial role in fighting viral infections. However, the ORF8 protein of the virus evade the immune system by interacting with IRF3, hindering its nuclear translocation and consequently downregulate the type I IFN signaling pathway. To block the binding of ORF8–IRF3 and inhibit viral pathogenesis a quick discovery of an inhibitor molecule is needed. Therefore, in the present study, the interface between the ORF8 and IRF3 was targeted on a high-affinity carbon nanotube by using computational tools. After analysis of 62 carbon nanotubes by multiple docking with the induced fit model, the top five compounds with high docking scores of -7.94 kcal/mol, -7.92 kcal/mol, -7.28 kcal/mol, -7.19 kcal/mol and -7.09 kcal/mol (top hit1-5) were found to have inhibitory activity against the ORF8–IRF3 complex. Molecular dynamics analysis of the complexes revealed the high compactness of residues, stable binding, and strong hydrogen binding network among the ORF8–nanotubes complexes. Moreover, the total binding free energy for top hit1-5 was calculated to be -43.21 ± 0.90 kcal/mol, -41.17 ± 0.99 kcal/mol, -48.85 ± 0.62 kcal/mol, -43.49 ± 0.77 kcal/mol, and -31.18 ± 0.78 kcal/mol respectively. These results strongly suggest that the identified top five nanotubes (hit1-5) possess significant potential for advancing and exploring innovative drug therapies. This underscores their suitability for subsequent in vivo and in vitro experiments, marking them as promising candidates worthy of further investigation.

Keywords SARS-CoV-2, ORF8, IRF3, Nanotubes, Molecular simulation

[†]Muhammad Suleman and Abbas Khan contributed equally to this work.

*Correspondence:

Hadi M. Yassine
hyassine@qu.edu.qa
Sergio Crovella
sgrovella@qu.edu.qa

Full list of author information is available at the end of the article



© The Author(s) 2024. **Open Access** This article is licensed under a Creative Commons Attribution 4.0 International License, which permits use, sharing, adaptation, distribution and reproduction in any medium or format, as long as you give appropriate credit to the original author(s) and the source, provide a link to the Creative Commons licence, and indicate if changes were made. The images or other third party material in this article are included in the article's Creative Commons licence, unless indicated otherwise in a credit line to the material. If material is not included in the article's Creative Commons licence and your intended use is not permitted by statutory regulation or exceeds the permitted use, you will need to obtain permission directly from the copyright holder. To view a copy of this licence, visit <http://creativecommons.org/licenses/by/4.0/>. The Creative Commons Public Domain Dedication waiver (<http://creativecommons.org/publicdomain/zero/1.0/>) applies to the data made available in this article, unless otherwise stated in a credit line to the data.

Introduction

The current COVID-19 pandemic, caused by SARS-CoV-2, is genetically connected to the SARS-CoV virus responsible for severe acute respiratory syndrome in 2002–2003, as well as other SARS-related viruses found in bats [1]. SARS-CoV-2's proteome consists of 12 distinct ORFs (open reading frames), which give rise to four structural proteins and twenty-two non-structural proteins [2]. Among the structural proteins are the nucleocapsid (N), membrane (M), envelope (E), and spike (S), while the non-structural proteins are encoded by ORF1ab and six accessory proteins (ORF3a, ORF6, ORF7a, ORF7b, ORF8, and ORF9), encompassing nsp 1–16 [3].

In the human defense system, the activation of the type 1 interferon (IFN) pathway contribute to abolish viral infection. The host pattern recognition receptors are actively involved in the identifications of pathogen-associated molecular patterns and activation of Interferon regulatory factor 3 (IRF3) [4]. In general, the IRF3 is normally present in the cytoplasm in an inactive state, however, during viral pathogenesis, the IRF3 is activated by phosphorylation and translocated to the nucleus [5]. In the nucleus, the activated IRF3 binds to conserved sequences known as IFN stimulated response elements to trigger the transcription of type I IFN genes which are necessary for the control of early viral infection [6, 7].

For effective infection, viruses, particularly coronaviruses, have developed a mechanism to inhibit IFN production by targeting distinct elements of IFN signaling [8]. By attaching to IRF3, viral proteins help coronaviruses in suppressing the host's innate immune system, by inhibiting the synthesis of IFN β [8–12]. Furthermore, RNA viruses particularly the SARS-CoV and SARS-CoV-2, are prone to rapid mutagenesis that enhanced the virus spread and infection [12].

ORF8 protein which contains 366 nucleotides and 121 amino acids is the most important SARS-CoV-2 accessory protein, and it is more prone to mutation [13]. ORF8 protein escapes the human immune system by binding to and reducing the nuclear translocation of IRF3 and hence downregulating the MHC-1 (major histocompatibility complex class I) [14] and the type I IFN signaling pathway [15–17]. The pathway is shown in the Fig. 1. Since the appearance of SARS-CoV-2, there have been various mutations detected in ORF8. These mutations, like L84S, V62L, S24L, and W45L, have been identified in various SARS-CoV-2 variants. Changes in ORF8 due to these mutations have influenced their ability to bind with IRF3. For instance, the W45L mutation showed increased affinity for IRF3, suggesting a heightened capacity for immune evasion [18].

Virtual drug screening, molecular dynamics (MD) simulation, and binding free energy calculation collectively

revolutionize drug discovery by offering efficient computational methodologies to identify and optimize potential drug candidates [19, 20]. Virtual screening accelerates the initial stages of drug discovery by swiftly evaluating large chemical libraries and prioritizing compounds for experimental testing based on predicted binding affinities [21]. MD simulations provide detailed insights into the dynamic behavior and structural flexibility of biomolecular systems, elucidating key interactions between ligands and their target proteins. Binding free energy calculations complement experimental data by quantitatively estimating the strength of ligand–protein interactions, guiding the rational design of more potent and selective drugs [22, 23]. Carbon nanotubes (CNTs) have a wide range of potential applications, including nanoelectronics, biosensors, biomolecular recognition devices, molecular transporters, cancer therapy, and diagnosis. Many studies have been done on the biological impacts of carbon nanotubes and concluded that the interactions of target proteins and CNTs (nanoparticle–protein corona) play important role in the control of biological activities [24]. Previously the carbon nanotubes were used against the HBx-Bcl-xL interface to halt the hepatitis B viral replication [25]. The same were also used to specifically target the RAN polymerase of the influenza A virus. These investigations revealed that such targeting could effectively impede both the infection by the influenza A virus and the expression of its nucleoprotein and nonstructural protein 1 [26]. The discovery of novel drugs by targeting the interface involved in the pathogenesis makes a significant contribution to the field of therapeutics development [27]. Since ORF8 protein participates in important cellular activities like binding to IRF3 and escaping the human immune system [16]. Therefore, in the current study, the high-affinity carbon nanotubes were used to target the ORF8 interface by using the virtual drug screening, molecular dynamic simulation and binding free energy calculation approaches. Using molecular docking and molecular dynamics simulation we target the interface of ORF8 to curtail the binding of this protein with the IRF3 and reduce the chances of SARS-CoV-2 infection.

Materials and methods

Data retrieval and preparation

The crystal structure of the ORF8 protein (PDB ID: 7jtl) was retrieved from the protein databank (<https://www.rcsb.org/structure/1p4q>) [28]. The GalaxyRefine online server was used for the energy minimization and refinements of the ORF8 protein structure. The GalaxyRefine online server enhances protein structures generated by modeling or prediction methods through a series of refinements including side-chain optimization, loop modeling, energy minimization, and molecular dynamics

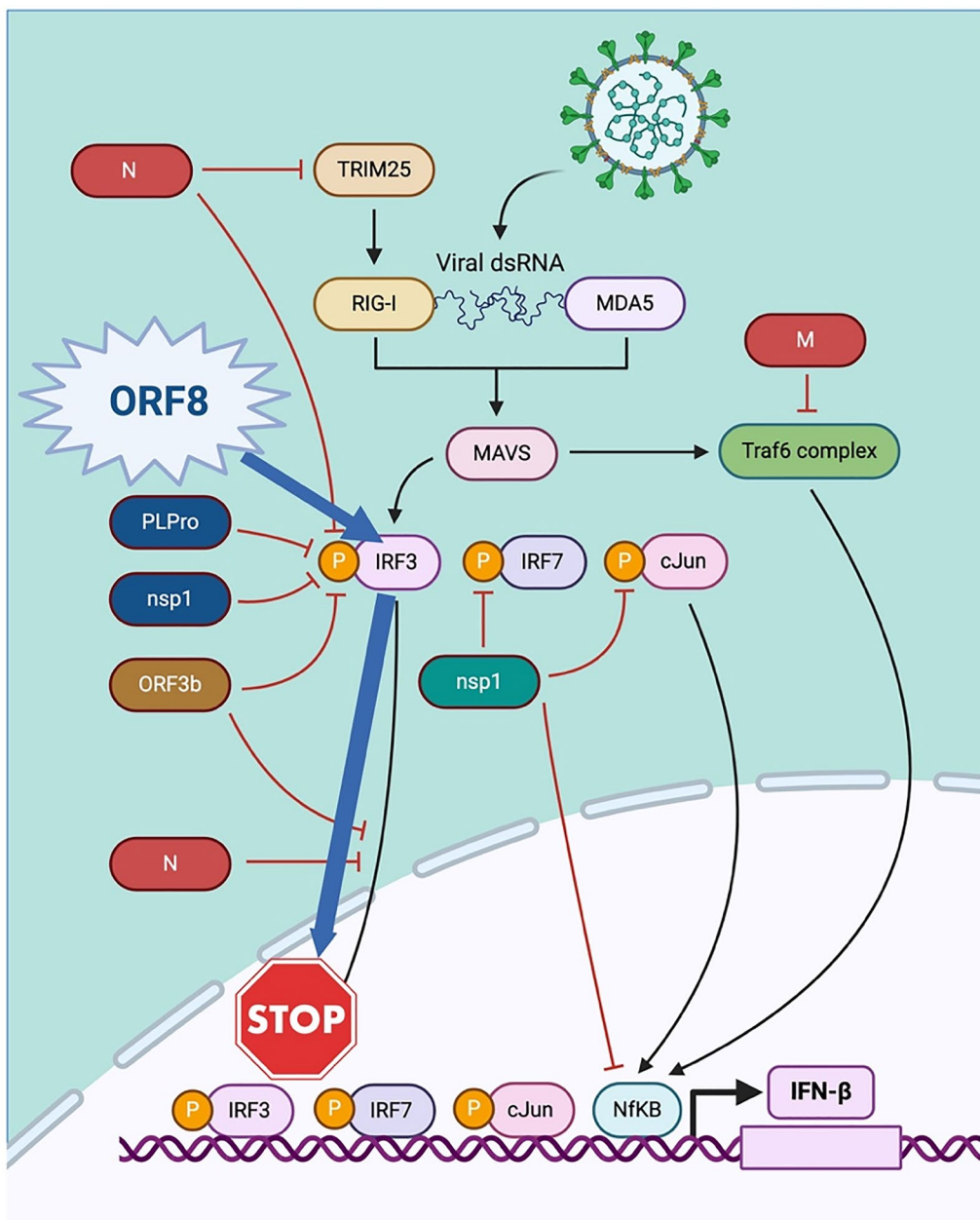


Fig. 1 Illustrating the function of ORF8 and IRF3 in immune evasion

simulations. By adjusting side-chain conformations and optimizing local geometry, GalaxyRefine aims to improve the overall quality and accuracy of protein models, reducing steric clashes and enhancing packing interactions [29]. To target the ORF8 binding interface we searched the literature and found 62 distinct carbon nanotubes which have the favorable properties and used previously against the biological targets in different diseases [30]. Then the PyRx tool was used for the arrangement and minimization of identified nanotubes [31].

Screening of carbon nanotubes against ORF8 interface

After preparing all the retrieved nanotubes were tested against the previously identified interface of ORF8 protein used for binding with the IRF3 protein. The residues 62–85 of ORF8 are reported to be responsible for binding with the IRF3 protein. Therefore, these interface residues were selected for binding with the nanotubes. Before commencing virtual screening with EasyDock Vina 2.0, all nanotubes were converted into the.pdbqt format. The ligands were transformed into pdbqt

structures, meticulously assigning their atomic charges and atom types using advanced tools like Open Babel. Special attention was paid to non-polar hydrogen atoms, Gasteiger charges, and identifying torsion tree roots necessary for subsequent flexibility analysis of the ligands. On the other hand, preparing the receptor involved generating grid maps with AutoGrid, a crucial step in defining the docking space. This complex process included setting grid dimensions, determining appropriate spacing parameters, and preparing the macromolecule in pdbqt format. Additionally, the receptor was enhanced with hydrogen atoms, charge assignments, and atom type specifications to ensure compatibility with subsequent docking procedures. This software offers an intuitive graphical interface for efficiently screening virtual databases. The screening process utilized the AUTODOCK4 algorithm to evaluate and prioritize potential nanotube candidates. To expedite the initial screening, a lower exhaustiveness setting of 16 was chosen. Following this, the most promising compounds were subjected to a second screening with a higher exhaustiveness value of 64. This phase was undertaken to eliminate false-positive results and reassess the compounds that ranked highest based on their scores [32]. Based on high scores, the best hits were processed for the redocking and rescoring.

Induced-fit Docking (IFD) of the top hits

In the following phase, the shortlisted compounds with high scores underwent a rigorous screening process known as induced fit docking (IFD), employing an exhaustive 64-step approach. This method utilized AutoDockFR, which utilizes the AutoDock4 scoring function and has been enhanced to improve the success rate of the docking process [33]. During cross-validation docking experiments, it was observed that AutoDockFR exhibited superior accuracy in identifying docking poses and notably outperformed AutoDock Vina in terms of speed without compromising precision.

Molecular dynamics simulation of the top hits

The molecular dynamics simulation of the selected top hits docking complexes employed the Amber20 package [34]. The simulation incorporated the amber GAFF (general force field) and ff14SB forcefield for the complexes, with drug topologies generated using the antechamber module. Subsequently, each system underwent solvation and neutralization using a TIP3P water box and Na⁺ counter ions. A two-step energy minimization procedure was utilized, succeeded by a process involving heating and equilibration. The Particle Mesh Ewald (PME) method [35] was employed to calculate long-range electrostatic interactions. Van der Waals contacts and short-range Coulombic interactions were considered within a

cut-off range of 1.4 nm. Temperature was maintained at 300 K using a Langevin thermostat, while pressure control utilized a Berendsen barostat. The simulation duration for each complex was 50 ns (50 ns), employing a time step of 2 fs. CPPTRAJ and PTRAJ tools were employed to evaluate dynamics, stability, and other characteristics of the ligand–protein complexes [36, 37].

Post simulation analysis

The analysis of the tophits-ORF8 complexes involved using CPPTRAJ and PTRAJ software packages to evaluate various structural properties [37]. To assess compactness, dynamic stability, average hydrogen bond formation, and flexibility, specific calculations were employed. Radius of gyration (Rg) was computed to measure structural compactness, employing the formula:

$$r_{RG}^2 = \frac{\sum_{i=1}^N m_i (\mathbf{r}_i - \mathbf{r}_{CM})^2}{\sum_{i=1}^N m_i} \quad (1)$$

where r_i represents the position of the atom at index i , m_i is its mass, r_{CM} is the center of mass, N is the total number of atoms, and r_{2RG} is the squared radius of gyration. To measure structural stability over the simulation, Root Mean Square Deviation (RMSD) was calculated using:

$$RMSD = \sqrt{\frac{1}{N} \sum_{i=1}^N \delta_i^2} \quad (2)$$

δ_i^2 refers to the squared disparity between the position of an atom at index i and its position in the reference structure, while N represents the total number of atoms.

For investigating individual residue-level flexibility, Root Mean Square Fluctuation (RMSF) computations were employed. RMSF evaluates residue fluctuations rather than overall complex positional changes. The RMSF was determined via the formula:

$$B = \frac{8\pi^2}{3} \Delta r^2 \quad (3)$$

where B represent the B-factor or thermal factor and Δr^2 is the mean square deviation. To obtain RMSF while considering the three spatial dimensions, the rearranged equation is used:

$$RMSF = \sqrt{\frac{3B}{8\pi^2}} \quad (4)$$

The binding free energy calculations

The MMPBSA.PY script was utilized to compute the binding free energy of individual protein–ligand complexes, incorporating 2500 snapshots [38–41]. This

approach for estimating free energy is widely adopted in diverse research to measure the total binding energy (TBE) of different ligands across various studies [42–44]. The binding free energy was calculated for receptors ($G_{receptor, solvated}$), unbound states of ligand ($G_{ligand, solvated}$) and for each complex ($G_{complex, solvated}$). Expanding on this, Equation can be expressed as follows:

$$\Delta G_{bind} = G_{(complex, solvated)} - G_{(ligand, solvated)} - G_{(receptors, solvated)} \quad (5)$$

To delve deeper into the specific energy contributions, we reformulated Equation as:

$$G = E_{MolecularMechanics} - G_{solvated} - TS \quad (6)$$

To calculate the specific energy term, the formula was restructured as follows:

$$\begin{aligned} \Delta G_{bind} &= \Delta E_{MolecularMechanics} + \Delta G_{solvated} - \Delta TS \\ &= \Delta G_{vacuum} + \Delta G_{solvated} \end{aligned} \quad (7)$$

$$\Delta E_{MolecularMechanics} = \Delta E_{int} + \Delta E_{electrostatic} + \Delta E_{vdW} \quad (8)$$

$$\Delta G_{solvated} = \Delta G_{Generalizedborn} + \Delta G_{surfacearea} \quad (9)$$

$$\Delta G_{surfacearea} = \gamma \cdot SASA + b \quad (10)$$

The overall binding energy comprises several components. The ΔG_{bind} represents the protein–protein, protein–ligand and protein nucleic acid associated free energy. The ΔE_{MM} denoted the overall gas phase energy. Solvation entails the combined effects of polar ($\Delta G_{PB/GB}$) and nonpolar (ΔG_{GSA}) components. The polar contribution, $\Delta G_{PB/GB}$, is typically determined through Poisson–Boltzmann (PB) or generalized Born (GB) methods, while ΔG_{GSA} represents the nonpolar solvation free energy and is often derived from a linear function of solvent-accessible surface area (SASA).

Bioavailability, metabolism, and potential toxicity analysis of top hits

For evaluating the Absorption, Distribution, Metabolism, Excretion, Toxicity (ADMET) properties of top hit nanotubes, we employed the admetSAR online tool (<http://lmmd.ecust.edu.cn/admetSar2>). AdmetSAR is a comprehensive resource providing the latest data on diverse chemicals and their Absorption, Distribution, Metabolism, Excretion, and Toxicity profiles. Its user-friendly interface enables searching by name, CASRN, and similarity. Moreover, admetSAR utilizes the ADMET-Simulator, a cutting-edge chemoinformatics toolbox, to predict approximately 50 ADMET endpoints using highly accurate QSAR models [45].

Results and discussion

Structural retrieval and pre-processing

ORF8 protein which contains 366 nucleotides and 121 amino acids is the most important SARS-CoV-2 accessory protein, and it is more prone to mutation [13]. In the human defense system, the activation of the type 1 interferon (IFN) pathway contributes to eliminate viral infection. However, a recent study reported that ORF8 protein escapes the human immune system by binding to and reducing the nuclear translocation of IRF3 and hence downregulating the MHC-1 (major histocompatibility complex class I) [14] and the type I IFN signaling pathway [15–17]. The overall pathway is shown in the Fig. 1. Due to the critical role of ORF8 protein in the human immune system evasion, it could be an important drug target in the therapeutic development of SARC-CoV-2 infection. Therefore, the current study was designed to screen the high-affinity carbon nanotubes against the ORF8–IRF3 interface to block its binding and halt immune evasion by SARC-CoV-2. The 3D structure of ORF8 (PDB ID: 7JX6) was retrieved from the protein databank (<https://www.rcsb.org/structure/1p4q>) [28]. Then the structure was minimized and prepared before the screening of carbon nanotubes. The overall work flow of this study is shown in the Fig. 2.

Screening of ORF8–IRF3 binding interface with carbon nanotube

Carbon nanotubes (CNTs) possess extensive potential applications spanning nanoelectronics, biosensors, biomolecular recognition devices, molecular transporters, and cancer diagnosis and therapy [46]. Numerous investigations have focused on the biological effects of carbon nanotubes, revealing that the interplay between CNTs and target proteins (referred to as nanoparticle–protein corona) significantly influences biological functionalities [47, 48]. A total of 62 carbon nanotubes (fullerenes) were collected from various sources and screened against the ORF8–IRF3 binding interface using the PyRx virtual screening approach. Before docking, the ligand molecules were arranged and the binding interface residues (aa 62–85) of ORF8 were defined for the docking as shown in Fig. 3a. The two-step approach was used for the screening of collected nanotubes with ORF8 proteins. In the first step, the score range was set to -7.41 to -4.36 kcal/mol, and screened all the 62 carbon fullerenes. Then in the next step, the induced-fit docking approach with 64 exhaustiveness was carried out to screen the 13 highest scoring compounds to confirm the best final hits. For IDF, to improve the success rate of docking, the ADFR (AutoDcokFR–AutoDock for Flexible Receptor) which utilized the AutoDock4 algorithm was used. The ADFR lowers the internal energy of the receptor and also

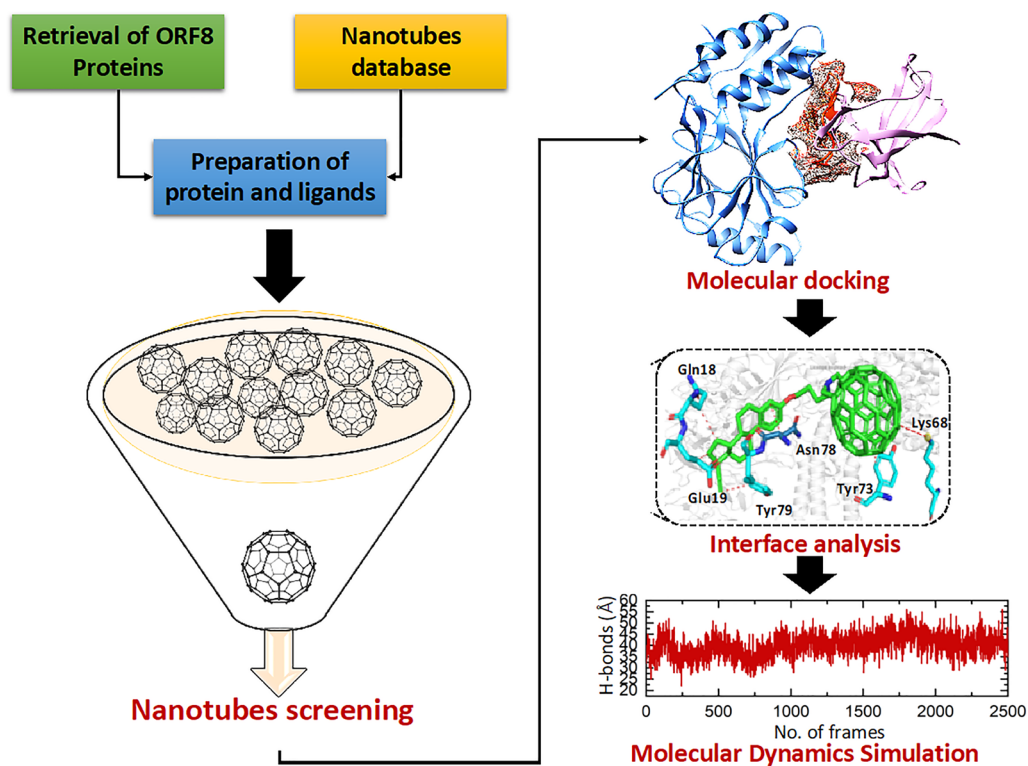


Fig. 2 The figure showing the overall work flow of the study such as screening of nanotubes, molecular docking and molecular dynamic simulation

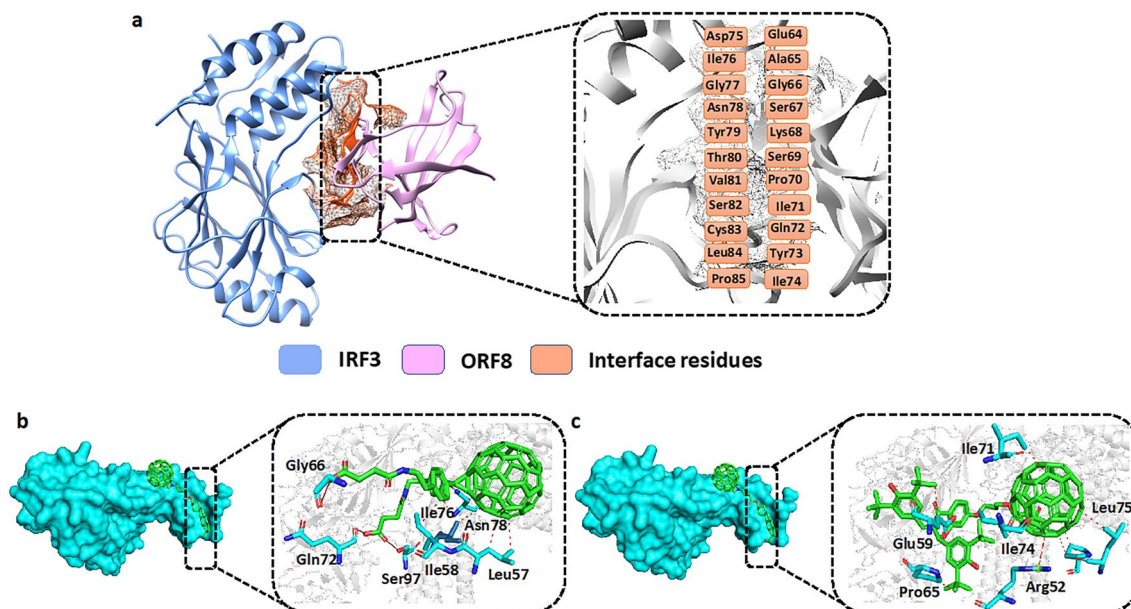


Fig. 3 a showing interface residues of ORF8 with IRF3. b Showing the interactions of best hit1 with ORF8 residues. c Showing the interactions of best hit2 with ORF8 residues. The green color represents the best hits while the cyan color represents the interacting residues of ORF8

optimized the confirmation of the receptor side chain. Finally, for shortlisting the best final hits the range of binding energy was set to > -7.0 kcal/mol. By using the

aforementioned parameters, the IFD docking found only 5 compounds having binding free energy > -7.0 kcal/mol. The docking scores of the first two best compounds

were reported to be -7.94 and -7.92 kcal/mol, respectively. As shown in Fig. 3b the best hit 1 formed 3 hydrogen bonds with Gly66, Gln72, Ser97, and 6 hydrophobic bonds with the Gly66, Gln72, Ser97, and Leu57, Ile58, Ile76, Asn78 residues. However, the best hit 2 (Fig. 3c) established 1 hydrogen bond with Arg52 and 7 hydrophobic bonds with, Glu59, Pro65, Ile71, Ile74, and Leu75 residues. In conclusion, both the top hit 1 and 2 targeted the specific residues involved in the interaction with the IRF3. For instance, the top hit 1 targeted the Gly66 and Gln72, while Hit 2 targeted Pro65, Ile71, and Ile74 key residues crucial for the ORF8–IRF3 interaction. This targeted binding may impede ORF8's interaction with IRF3 by blocking these critical residues. The interactions of compounds 1 and 2 with the ORF8 residues are shown in Fig. 3.

Afterward, compound 3 (best hit 3) with a docking score of -7.28 kcal/mol showed a similar pattern of contacts with the ORF8 binding interface with 1 cation (Lys68) and 5 hydrophobic interactions (Gln18, Glu19, Tyr73, Asn78, Tyr79). Moreover, the docking score of best hit4 was reported to be -7.19 kcal/mol and established 4 hydrogen (Leu60, Glu64, Ala65, Gly77) and 6 hydrophobic bonds (Leu57, Ile58, Ala65, Ile76) with the ORF8 interface residues. Finally, with a docking score of -7.09 kcal/mol the best hit5 established 6 hydrophobic interactions with Ile58, Val62, Lys68, Tyr73, Asn78 and Tyr79 amino acid residues. In summary, these top hits also targeted the specific residues of ORF8 such as Glu64, Ala65, Lys68, and Tyr73 that are involved in the binding with IRF3. Our results revealed high specific binding of the shortlisted nanotubes with the interface residues of ORF8 which may lead to the inhibition of the interaction

between the ORF8 and IRF3. The binding network of best hits 3, 4, and 5 with the residues of the ORF8 interface are shown in Fig. 4.

Evaluation of dynamic stability of ORF8-nanotube

The stability of molecular interactions within a binding cavity is a critical factor in finding the binding efficiency of small ligand molecule. This metric provides details on the dynamic stability of interacting molecules, which can shed light on the binding strength. Understanding a protein's dynamic stability is crucial in estimating the stability of biological complex in dynamics environment [49, 50]. To test the stability of ORF8-nanotube complexes in a dynamic environment 50 ns simulations were performed. The CPPTRAJ module of AMBER was applied to calculate the stability of complexes by several statistical parameters. For the said purpose, the RMSD (root mean square deviation) was calculated to check the actual deviation of a carbon atom from the original confirmation of docked complexes. The lower RMSD represents the higher complex stability whereas the higher RMSD shows lower stability. The average RMSD for the top hit 1–5 was 4.0 Å, 3.5 Å, 5.2 Å, 6.0 Å, and 4.0 Å respectively. According to the RMSD values, all complexes showed good stability with no major perturbations till 50 ns. The RMSD plot of top hit 1 was uniform until 33 ns with a minor perturbation at 15 ns however, a sudden rise of RMSD was depicted at 34 ns and then gained stability at 40 ns until 50 ns (Fig. 5a). The top hits 2 and 4 gained stability at 5 ns with a mean RMSD of 3.5 Å and 6 Å. Both complexes showed the highest stability with no global or local structural changes noticed until 50 ns (Fig. 5b, d). In the case of the top hit 3 the system equilibrated at 10 ns

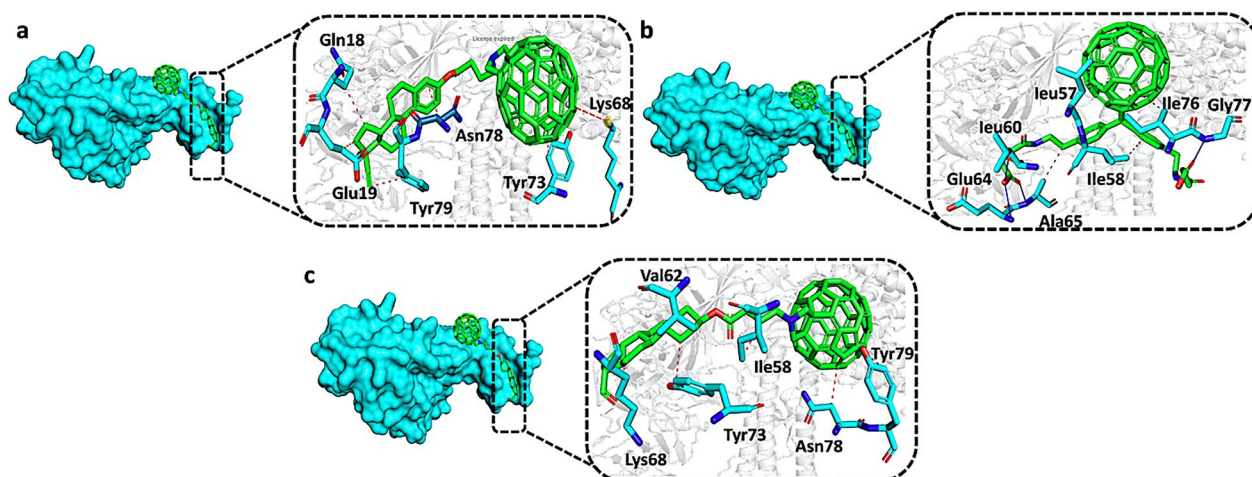


Fig. 4 a Showing the interactions of best hit3 with ORF8 residues. b Showing the interactions of best hit4 with ORF8 residues. c Showing the interactions of best hit5 with ORF8 residues. The green color represents the best hits while the cyan color represents the interacting residues of ORF8

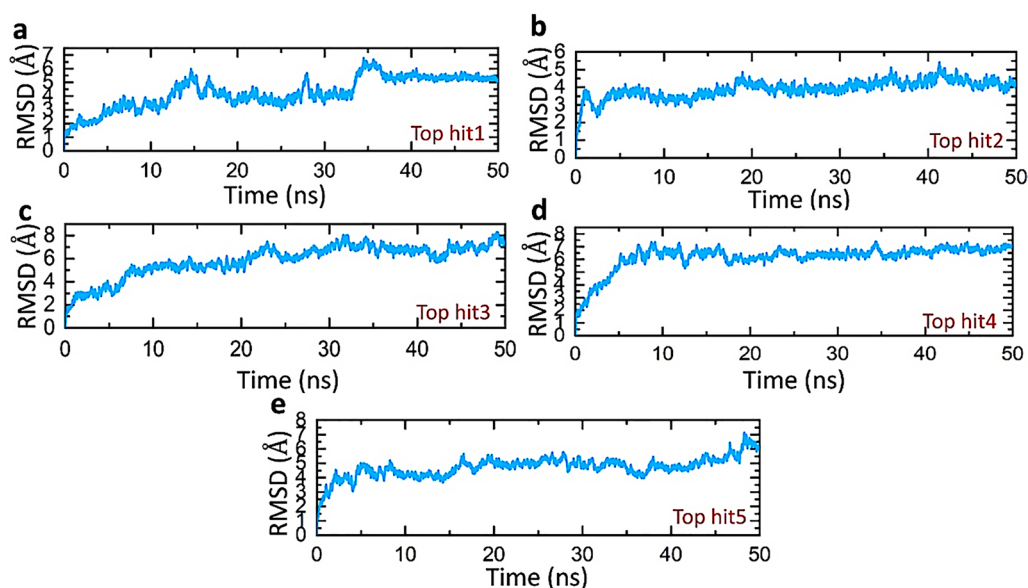


Fig. 5 Dynamic stability analysis of top hits-ORF8 complexes (a) represents the RMSD value of top hit 1-ORF8 complex (b) represents the RMSD value of top hit 2-ORF8 complex (c) represents the RMSD value of top hit 3-ORF8 complex (d) represents the RMSD value of top hit 4-ORF8 complex (e) represents the RMSD value of top hit 5-ORF8 complex

and then a steady increase was observed in the RMSD valued till 50 ns, however, there is no major fluctuations were seen after equilibration (Fig. 5c). Finally, the top hit 5 complexes gained stability at 5 ns and remained stable until 45 ns with no structural changes which are followed by minor deviation till 50 ns (Fig. 5e). The top hit 2, 4, and 5 showed a greater intermolecular affinity of ORF8 for the respective nanotubes and further validate the result of docking in terms of lowest energy and conformational stability. Figure 4 shows the RMSDs of all complexes.

Residual fluctuations analysis of top hits-ORF8 complexes

To identify the critical residues important for retaining the interacting ligand and overall stability of complex, understanding the systems flexibility at the residue level is indispensable. Understanding the system's flexibility at the residue level is critical for identifying residues that are critical for retaining the interacting ligand and overall complex stability [51, 52]. To analyze the residues fluctuation, we investigated the RMSF (root-mean-square fluctuation) of the target system. By comparing the Root Mean Square Fluctuation (RMSF) values of a protein with and without a drug, scientists can glean valuable insights into how the drug interacts with the protein and how it affects the protein's form and function. For instance, when the RMSF values of a protein are elevated in the presence of a drug, it could suggest that the drug triggers structural adjustments and enhances the protein's adaptability [53, 54]. Upon analyzing our findings, we observed an elevation in the Root Mean

Square Fluctuation (RMSF) of residues within the target site (80–100) following nanotube binding compared to the apo state. This suggests that the drug's binding induces heightened flexibility or movement in these residues, potentially to accommodate the ligand. The average RMSF value of all complexes is about 2 Å which further confirmed the results of RMSD and affirmed the high stability of all complexes. However, the residues present at N-terminal and C-terminal are showing instability which might be due to the highly flexible nature of protein ends [55]. Figure 6 shows the RMSF values of apo and all complexes.

Structural compactness analysis of top hits-ORF8 complexes

The radius of gyration serves as a crucial metric for assessing the interplay between a protein and a drug molecule. A reduced radius of gyration signifies a more compact arrangement of the protein and drug when they are bonded. This implies that the protein undergoes structural alterations upon binding with the drug, resulting in a tighter, more condensed structure [56]. It offers valuable information regarding the general configuration and density of the protein-drug combination. Therefore, analyzing the radius of gyration in a protein-drug complex can help gauge the effectiveness of drug binding and its subsequent influence on the protein's conformation [57]. To analyze the structural compactness of protein during the molecular dynamic simulation, we employed the Rg (radius of gyration) analysis. The Rg analysis

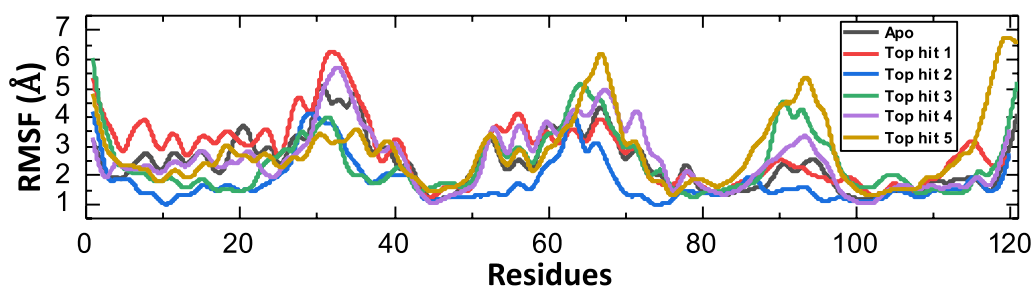


Fig. 6 Residues flexibility of all complexes calculated as RMSF

helped to identify whether the interacting residues in ORF8-nanotube complex are in equilibrium with a lower energy state and whether the residues are tightly bound to each other. Lower the Rg value higher will be the stability whereas a higher Rg indicates the instability of the system. As shown in Fig. 7a–e the average Rg values for the tophit1-5 were found to be 16.5, 17.7, 16.8, 16.6, and 17.6 respectively, however, some fluctuations in Rg values were found during the simulations due to the binding and unbinding of nanotubes with the ORF8 during this time.

Determining strength of intermolecular interactions

Hydrogen bonding plays a crucial role in the stability of binding complexes and the effective functioning of biological interactions. Evaluating the hydrogen bonds established in molecular interactions is a valuable method for assessing binding affinity [58]. A comprehensive comprehension of the hydrogen bonding configurations within protein-drug interactions is vital for making precise predictions about the strength of these

interactions [59, 60]. The final ORF8-nanotubes complexes were subjected to the hydrogen bonding analysis to calculate the number of hydrogen bonds in the frame during the MD simulations. As shown in Fig. 8 all the ORF8-nanotubes complexes have a strong network of hydrogen bonds which represent the stable interaction of nanotubes with the target ORF8. In each frame, the average hydrogen bonds in each complex were recorded to be 45, 43, 38, 43, and 40 respectively. The above results of hydrogen bonding counter verify the results of RMSD and RMSF in terms of complex stability. Figure 8 shows the hydrogen bonds of all complexes.

Binding free energy calculations of top hits-ORF8 complexes

Assessing the binding energy is crucial for re-evaluating the binding conformation and verifying the accuracy of the interacting components. This approach offers superior accuracy and is cost-effective compared to wet lab experiments. Previously, it has been utilized to ascertain

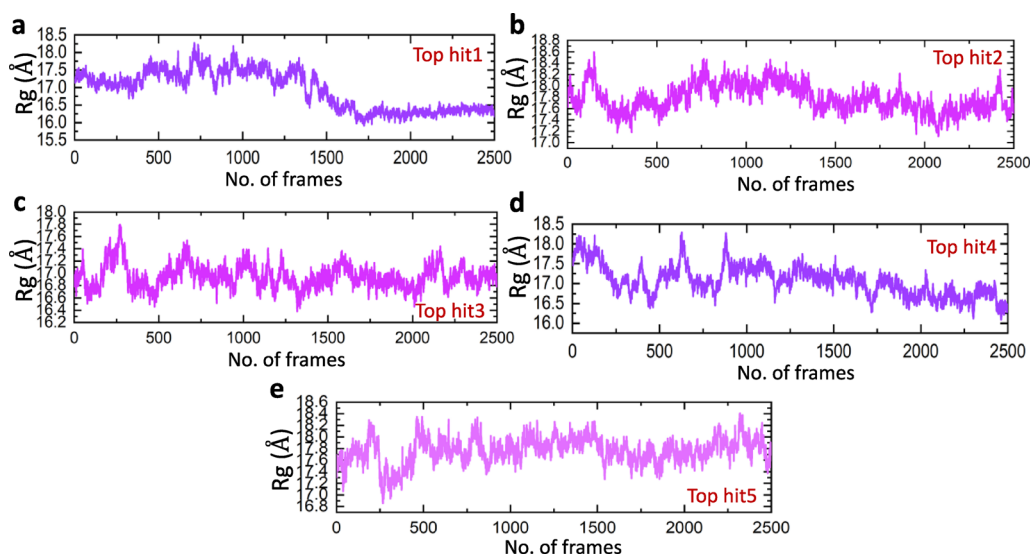


Fig. 7 Calculation of Rg for all complexes. **a** showing the Rg value of top hit 1, **b** showing the Rg value of top hit 2, **c** showing the Rg value of top hit 3, **d** showing the Rg value of top hit 4, **e** showing the Rg value of top hit 5

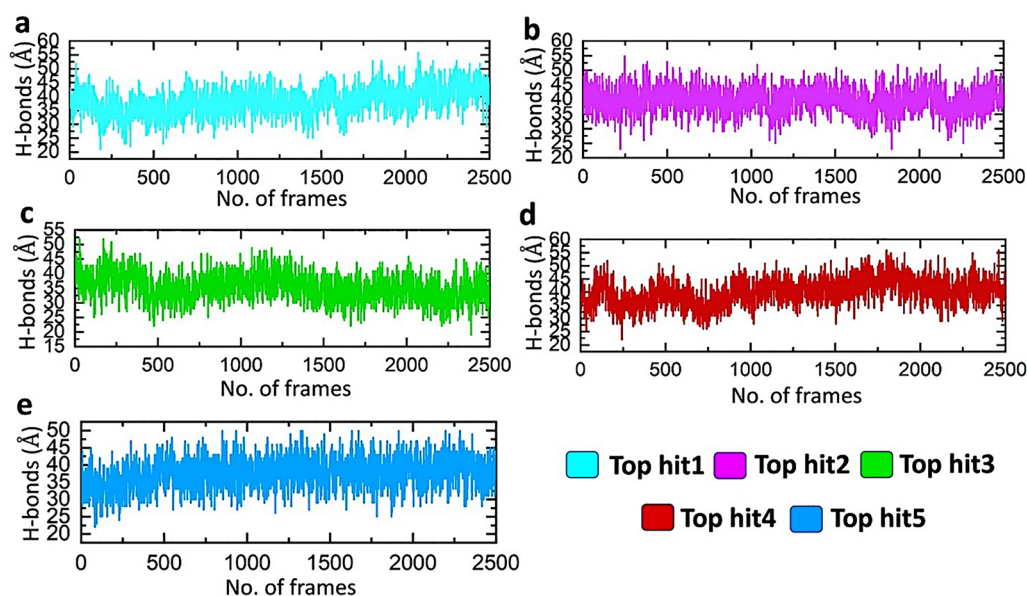


Fig. 8 The hydrogen bonding network of all complexes. **a** showing the average hydrogen bonds for top hit 1-ORF8 complex, **b** showing the average hydrogen bonds for top hit 2-ORF8 complex, **c** showing the average hydrogen bonds for top hit 3-ORF8 complex, **d** showing the average hydrogen bonds for top hit 4-ORF8 complex, **e** showing the average hydrogen bonds for top hit 5-ORF8 complex

the binding energy of small molecules that target receptors and druggable proteins of SARS-CoV-2 [55, 61, 62]. Given the method's broad applicability, we've computed the binding free energy for the top five candidates utilizing MD trajectories. The computed Van der Waals energy values for the top-ranking complexes, specifically complexes 1 through 5, demonstrated a distinct stability stemming from intermolecular forces. These recorded values were as follows: -49.49 ± 1.09 kcal/mol, -55.58 ± 1.19 kcal/mol, -55.43 ± 0.69 kcal/mol, -54.50 ± 0.71 kcal/mol, and -41.84 ± 0.84 kcal/mol for their respective complexes. These figures emphasize the attractive forces generated by Van der Waals interactions among the molecules, shedding light on the stability and affinity of these complexes. In addition, the electrostatic energy calculations for these same complexes provide insights into their charged interactions. The computed electrostatic energy values are

as follows: -1.93 ± 0.80 kcal/mol, 58.72 ± 2.37 kcal/mol, -5.52 ± 0.52 kcal/mol, 26.23 ± 2.66 kcal/mol, and 118.97 ± 9.71 kcal/mol, revealing the extent to which electrostatic forces contribute to the overall binding energy. Furthermore, the binding free energies for ESURE, EGB, Delta G Gas, and Delta G Solv have been determined and are presented in Table 1. The total binding free energy for each hit was calculated to be -43.21 ± 0.90 kcal/mol for hit1, -41.17 ± 0.99 kcal/mol for hit2, -48.85 ± 0.62 kcal/mol for hit3, -43.49 ± 0.77 kcal/mol for hit4, and -31.18 ± 0.78 kcal/mol for hit5. The total binding energy is mainly contributed by the vdW while in some complexes the electrostatic energies were observed to contribute to the total binding energy. Similar range of values has been previously reported for the drug-protein interactions which further validate our results of binding free energy [20, 27, 63].

Table 1 Binding free energy computation for the top hits using MM/GBSA method

| Parameters | Top hit 1 | Top hit 2 | Top hit 3 | Top hit 4 | Top hit 5 |
|--------------|-------------------|-------------------|-------------------|-------------------|--------------------|
| VDWAALS | -49.49 ± 1.09 | -55.58 ± 1.19 | -55.43 ± 0.69 | -54.50 ± 0.71 | -41.84 ± 0.84 |
| EEL | -1.93 ± 0.80 | 58.72 ± 2.37 | -5.52 ± 0.52 | 26.23 ± 2.66 | 118.97 ± 9.71 |
| EGB | 13.35 ± 0.49 | -39.76 ± 2.01 | 18.62 ± 0.55 | -10.15 ± 2.46 | -103.63 ± 8.86 |
| ESURF | -4.74 ± 0.03 | -4.19 ± 0.03 | -4.50 ± 0.03 | -5.05 ± 0.08 | -4.68 ± 0.12 |
| DELTA G gas | -51.82 ± 0.64 | 2.79 ± 1.73 | -62.96 ± 0.69 | -28.27 ± 2.85 | 77.12 ± 9.46 |
| DELTA G solv | 8.60 ± 0.52 | -43.96 ± 1.99 | 14.11 ± 0.53 | -15.21 ± 2.47 | -108.31 ± 8.80 |
| DELTA TOTAL | -43.21 ± 0.90 | -41.17 ± 0.99 | -48.85 ± 0.62 | -43.49 ± 0.77 | -31.18 ± 0.78 |

Table 2 Bioavailability, metabolism, and potential toxicity analysis of top hits

| ADMET properties | Top hit 1 | Top hit 2 | Top hit 3 | Top hit 4 | Top hit 5 |
|-----------------------------|-----------|-----------|-----------|-----------|-----------|
| Oral bioavailability | Yes | No | No | Yes | No |
| Water solubility | -4.173 | -3.889 | -2.964 | -4.173 | -3.153 |
| Human Intestinal Absorption | Yes | Yes | Yes | Yes | Yes |
| Blood–Brain Barrier | Yes | No | Yes | Yes | Yes |
| Carcinogenicity | No | No | No | No | No |
| Eye irritation | No | No | No | No | No |
| Hepatotoxicity | Yes | No | No | Yes | No |
| Nephrotoxicity | No | No | No | No | No |
| Respiratory toxicity | Yes | No | Yes | Yes | Yes |
| skin sensitization | No | No | No | No | No |
| OCT2 substrate | No | No | No | No | No |

Analysis of ADMET properties for the selected top hits

ADMET properties analysis is essential for drug design as it enables early identification of compounds with favorable pharmacokinetic and toxicological profiles, reducing the risk of late-stage failures and optimizing drug efficacy. By assessing factors such as absorption, distribution, metabolism, excretion, and toxicity, researchers can enhance drug safety, comply with regulatory standards, and predict clinical outcomes more accurately [64, 65]. Therefore, we proceeded to assess the ADMET properties of our chosen leading compounds utilizing the AdmetSAR online tool. Upon conducting oral bioavailability analysis, it was discerned that top hit 1 and top hit 4 possess the desirable attribute of oral bioavailability, while the remaining candidates lack this property. Notably, the efficacy of drug absorption hinges on water solubility, with heightened solubility indicating enhanced absorption features and heightened bioavailability [66]. Analysis of water solubility indicated that all the top hits displayed remarkably high solubility in water, achieving scores of -4.173, -3.889, -2.964, -4.173, and -3.153 for hits 1 through 5, respectively. Notably, all these top hits exhibited exceptional intestinal absorption rates of 100%. While most top hits effectively penetrated the blood–brain barrier, top hit 2 stood out as an exception. It is noteworthy that none of the identified top hits demonstrated carcinogenicity, eye irritation, nephrotoxicity, or skin sensitization. However, both top hit 1 and top hit 4 were associated with hepatotoxicity. Additionally, respiratory toxicity was observed across all top hits except for top hit 2. Despite the importance of the organic cation transporter 2 (OCT2) substrate in renal clearance enhancement, none of the compounds demonstrated activity as OCT2 substrates. Comprehensive ADMET properties of the top hits are summarized in Table 2.

Conclusions

In the stride toward combating the SARS-CoV-2, this study harnessed the power of Nano medicine-based approaches to unravel the pharmacological impact of carbon-based nanotubes. A strategic focus on the ORF8 interface emerged as a beacon of hope, a pivotal move in salvaging the host immune response. Within this molecular theater, five Nano carbons took center stage, demonstrating binding propensity against the essential residues—a promising ensemble of viral adversaries met with precision and efficacy.

The study's narrative seamlessly transitioned into the intricate realm of molecular simulations. The binding free energy, a measure of the molecular forces at play, underscored the robust and favorable interactions between the identified Nano carbons and their viral counterparts.

Yet, this culmination marks not a conclusion but a prelude to the next act. The identified compounds, having displayed prowess in the virtual domain, now beckon the tangible realities of *in vitro* and *in vivo* validation. The laboratory and living organisms stand as arenas where these Nano protagonists shall undergo rigorous scrutiny, their efficacy and safety scrutinized in the relentless pursuit of a COVID-19 treatment breakthrough.

Acknowledgements

Authors are thankful to the Researchers Supporting Project number (RSPD2024R1035), King Saud University, Riyadh, Saudi Arabia.

Author contributions

M.S and A.K conceptualized the study. M.S, K.I, A.K and Z.A generated the data. M.S, Z.A, D.W and N.A.A prepared the figures. A.K, N.A.A and H.M.Y provided computational resources. M.S and S.C wrote the main manuscript. D.W, H.M.Y and S.C supervised the experiments. All authors reviewed the manuscript.

Funding

This work was supported by Qatar University grant No. QUPD CAS-23-24491 and QUCG LARC 22/23-499.

Availability of data and materials

The data are available from the corresponding author on reasonable request.

Declarations**Ethics approval and consent to participate**

Not applicable.

Consent for publication

Not applicable.

Competing interests

The authors declare no competing interests.

Author details

¹Laboratory of Animal Research Center (LARC), Qatar University, Doha, Qatar. ²Center for Biotechnology and Microbiology, University of Swat, Swat, Pakistan. ³Department of Intensive Care Unit, Affiliated Hospital of Guangdong Medical University, Zhanjiang 524000, China. ⁴Services Institute of Medical Sciences, Lahore, Pakistan. ⁵Department of Bioinformatics and Biological Statistics, School of Life Sciences and Biotechnology, Shanghai Jiao Tong University, Shanghai 200240, People's Republic of China. ⁶School of Medical and Life Sciences, Sunway University, 47500 Sunway City, Malaysia. ⁷Department of Pharmacology and Toxicology, College of Pharmacy, King Saud University, Post Box 2455, 11451 Riyadh, Saudi Arabia. ⁸Biomedical Research Center, Qatar University, 2713 Doha, Qatar. ⁹College of Health Sciences-QU Health, Qatar University, 2713 Doha, Qatar.

Received: 13 January 2024 Accepted: 11 April 2024

Published online: 11 May 2024

References

- Ceraolo C, Giorgi FM. Genomic variance of the 2019-nCoV coronavirus. *J Med Virol.* 2020;92(5):522–8.
- Wang MY, et al. SARS-CoV-2: structure, biology, and structure-based therapeutics development. *Front Cell Infect Microbiol.* 2020;10:587269.
- Wu S, et al. Effects of SARS-CoV-2 mutations on protein structures and intraviral protein–protein interactions. *J Med Virol.* 2021;93(4):2132–40.
- Chen X, et al. SARS coronavirus papain-like protease inhibits the type I interferon signaling pathway through interaction with the STING-TRAF3-TBK1 complex. *Protein Cell.* 2014;5(5):369–81.
- Sharma S, et al. Triggering the interferon antiviral response through an IKK-related pathway. *Science.* 2003;300(5622):1148–51.
- Kawai T, Akira S. Antiviral signaling through pattern recognition receptors. *J Biochem.* 2007;141(2):137–45.
- Ivashkiv LB, Donlin LT. Regulation of type I interferon responses. *Nat Rev Immunol.* 2014;14(1):36–49.
- Lim YX, et al. Human coronaviruses: a review of virus–host interactions. *Diseases.* 2016;4(3):26.
- Wathelet MG, et al. Severe acute respiratory syndrome coronavirus evades antiviral signaling: role of nsp1 and rational design of an attenuated strain. *J virol.* 2007;81(21):11620–33.
- Huang C, et al. SARS coronavirus nsp1 protein induces template-dependent endonucleolytic cleavage of mRNAs: viral mRNAs are resistant to nsp1-induced RNA cleavage. *PLoS Pathog.* 2011;7(12):e1002433.
- Zhong Y, Tan YW, Liu DXJV. Recent progress in studies of arterivirus-and coronavirus-host interactions. *Viruses.* 2012;4(6):980–1010.
- Liu DX, et al. Accessory proteins of SARS-CoV and other coronaviruses. *Antiviral Res.* 2014;109:97–109.
- Pereira F. Evolutionary dynamics of the SARS-CoV-2 ORF8 accessory gene. *Infect Genet Evol.* 2020;85:104525.
- Zhang Y, et al. The ORF8 protein of SARS-CoV-2 mediates immune evasion through down-regulating MHC-I. *Proc Natl Acad Sci.* 2021;118(23):e2024202118.
- Li J-Y, et al. The ORF6, ORF8 and nucleocapsid proteins of SARS-CoV-2 inhibit type I interferon signaling pathway. *Virus Res.* 2020;286:198074.
- Rashid F, et al. The ORF8 protein of SARS-CoV-2 induced endoplasmic reticulum stress and mediated immune evasion by antagonizing production of interferon beta. *Virus Res.* 2021;296:198350.
- Flower TG, et al. Structure of SARS-CoV-2 ORF8, a rapidly evolving immune evasion protein. *Proc Natl Acad Sci.* 2021;118(2): e2021785118.
- Rashid F, et al. Roles and functions of SARS-CoV-2 proteins in host immune evasion. *Front Immunol.* 2022;13: 940756.
- Singh R, Bhardwaj VK, Purohit R. Inhibition of nonstructural protein 15 of SARS-CoV-2 by golden spice: a computational insight. *Cell Biochem Funct.* 2022;40(8):926–34.
- Singh R, Bhardwaj VK, Purohit R. Potential of turmeric-derived compounds against RNA-dependent RNA polymerase of SARS-CoV-2: an in-silico approach. *Comput Biol Med.* 2021;139: 104965.
- Singh R, et al. Identification of potential plant bioactive as SARS-CoV-2 Spike protein and human ACE2 fusion inhibitors. *Comput Biol Med.* 2021;136: 104631.
- Singh R, Purohit R. Multi-target approach against SARS-CoV-2 by stone apple molecules: a master key to drug design. *Phytother Res.* 2024;38(1):7–10.
- Sharma J, et al. An in-silico evaluation of different bioactive molecules of tea for their inhibition potency against non structural protein-15 of SARS-CoV-2. *Food Chem.* 2021;346: 128933.
- Ge C, et al. Binding of blood proteins to carbon nanotubes reduces cytotoxicity. *Proc Natl Acad Sci.* 2011;108(41):16968–73.
- Khan A, et al. Computational evaluation of abrogation of hbx-bcl-xl complex with high-affinity carbon nanotubes (Fullerene) to halt the hepatitis b virus replication. *Molecules.* 2021;26(21):6433.
- Shoji M, et al. Anti-influenza activity of c60 fullerene derivatives. *PLoS ONE.* 2013;8(6): e66337.
- Bhardwaj VK, et al. Identification of bioactive molecules from tea plant as SARS-CoV-2 main protease inhibitors. *J Biomol Struct Dyn.* 2021;39(10):3449–58.
- Koliopoulos MG, et al. Molecular mechanism of influenza A NS1-mediated TRIM25 recognition and inhibition. *Nat Commun.* 2018;9(1):1820.
- Heo L, Park H, Seok C. GalaxyRefine: Protein structure refinement driven by side-chain repacking. *Nucleic Acid Res.* 2013;41(W1):W384–8.
- Junaid M, et al. Analyses of the binding between water soluble C60 derivatives and potential drug targets through a molecular docking approach. *PLoS ONE.* 2016;11(2):e0147761.
- Dallakyan S, Olson AJ. Small-molecule library screening by docking with PyRx. In: *Chemical biology.* Springer; 2015. p. 243–50.
- Sayaf AM, et al. Pharmacotherapeutic potential of natural products to target the SARS-CoV-2 PLpro using molecular screening and simulation approaches. *Appl Biochem Biotechnol.* 2023;195:1–20.
- Ravindranath PA, et al. AutoDockFR: advances in protein-ligand docking with explicitly specified binding site flexibility. *PLoS Comput Biol.* 2015;11(12):e1004586.
- Case DA, et al. The Amber biomolecular simulation programs. *J Comput Chem.* 2005;26(16):1668–88.
- Price DJ, Brooks CL III. A modified TIP3P water potential for simulation with Ewald summation. *J Chem Phys.* 2004;121(20):10096–103.
- Suleman M, et al. Bioinformatics analysis of the differences in the binding profile of the wild-type and mutants of the SARS-CoV-2 spike protein variants with the ACE2 receptor. *Comput Biol Med.* 2021;138: 104936.
- Roe DR, Cheatham TE III. PTRAJ and CPPTRAJ: software for processing and analysis of molecular dynamics trajectory data. *J Chem Theory Comput.* 2013;9(7):3084–95.
- Sun H, et al. Assessing the performance of MM/PBSA and MM/GBSA methods. 4. Accuracies of MM/PBSA and MM/GBSA methodologies evaluated by various simulation protocols using PDBbind data set. *Phys Chem Chem Phys.* 2014;16(31):16719–29.
- Hou T, et al. Characterization of domain–peptide interaction interface: prediction of SH3 domain-mediated protein–protein interaction network in yeast by generic structure-based models. *J Proteome Res.* 2012;11(5):2982–95.
- Chen F, et al. Assessing the performance of the MM/PBSA and MM/GBSA methods 6 Capability to predict protein–protein binding free energies and re-rank binding poses generated by protein–protein docking. *Phys Chem Chem Phys.* 2016;18(32):22129–39.
- Miller BR III, et al. MMPBSA.py: an efficient program for end-state free energy calculations. *J Chem Theory Comput.* 2012;8(9):3314–21.

42. Chen J, et al. Decoding the identification mechanism of an SAM-III Riboswitch on ligands through multiple independent Gaussian-accelerated molecular dynamics simulations. *J Chem Inf Model.* 2022;62(23):6118–32.
43. Wang Y, et al. The systematic modeling studies and free energy calculations of the phenazine compounds as anti-tuberculosis agents. *J Biomol Struct Dyn.* 2019;37(15):4051–69.
44. Khan A, et al. Deep-learning-based target screening and similarity search for the predicted inhibitors of the pathways in Parkinson's disease. *RSC Adv.* 2019;9(18):10326–39.
45. Yang H, et al. AdmetSAR 2.0: web-service for prediction and optimization of chemical ADMET properties. *Bioinformatics.* 2019;35(6):1067–9.
46. Dai H. Carbon nanotubes: opportunities and challenges. *Surf Sci.* 2002;500(1–3):218–41.
47. Popov VN. Carbon nanotubes: properties and application. *Mater Sci Eng R Rep.* 2004;43(3):61–102.
48. Riviere JE. Pharmacokinetics of nanomaterials: an overview of carbon nanotubes, fullerenes and quantum dots. *Wiley Interdiscip Rev Nanomed Nanobiotechnol.* 2009;1(1):26–34.
49. Hollingsworth SA, Dror RO. Molecular dynamics simulation for all. *Neuron.* 2018;99(6):1129–43.
50. Karplus M, Kuriyan J. Molecular dynamics and protein function. *Proc Natl Acad Sci.* 2005;102(19):6679–85.
51. Rashid F, et al. Structural analysis on the severe acute respiratory syndrome coronavirus 2 non-structural protein 13 mutants revealed altered bonding network with TANK binding kinase 1 to evade host immune system. *Front Microbiol.* 2021;12:3575.
52. Shah A, et al. Comparative mutational analysis of SARS-CoV-2 isolates from Pakistan and structural-functional implications using computational modelling and simulation approaches. *Comput Biol Med.* 2022;141:105170.
53. Khan A, et al. Computational modelling of potentially emerging SARS-CoV-2 spike protein RBDs mutations with higher binding affinity towards ACE2: a structural modelling study. *Comput Biol Med.* 2022;141: 105163.
54. Rashid F, et al. Mutations in SARS-CoV-2 ORF8 altered the bonding network with interferon regulatory factor 3 to evade host immune system. *Front Microbiol.* 2021;12: 703145.
55. Khan A, et al. Higher infectivity of the SARS-CoV-2 new variants is associated with K417N/T, E484K, and N501Y mutants: an insight from structural data. *J Cell Physiol.* 2021;236(10):7045–57.
56. Khan S, et al. Proteome-wide mapping and reverse vaccinology-based B and T cell multi-epitope subunit vaccine designing for immune response reinforcement against *Porphyromonas gingivalis*. *J Biomol Struct Dyn.* 2022;40(2):833–47.
57. Suleman M, et al. Structural insights into the effect of mutations in the spike protein of SARS-CoV-2 on the binding with human furin protein. *Heliyon.* 2023;9(4):e15083.
58. Chen D, et al. Regulation of protein-ligand binding affinity by hydrogen bond pairing. *Sci Adv.* 2016;2(3): e1501240.
59. Chodera JD, Mobley DL. Entropy-enthalpy compensation: role and ramifications in biomolecular ligand recognition and design. *Annu Rev Biophys.* 2013;42:121–42.
60. Jewkes R, et al. Gender inequitable masculinity and sexual entitlement in rape perpetration South Africa: findings of a cross-sectional study. *PLoS ONE.* 2011;6(12): e29590.
61. Chen J, et al. Effect of mutations on binding of ligands to guanine riboswitch probed by free energy perturbation and molecular dynamics simulations. *Nucleic Acids Res.* 2019;47(13):6618–31.
62. Wang E, et al. End-point binding free energy calculation with MM/PBSA and MM/GBSA: strategies and applications in drug design. *Chem Rev.* 2019;119(16):9478–508.
63. Mohammad A, et al. Targeting SARS-CoV-2 macrodomain-1 to restore the innate immune response using in silico screening of medicinal compounds and free energy calculation approaches. *Viruses.* 2023;15(9):1907.
64. Wu F, et al. Computational approaches in preclinical studies on drug discovery and development. *Front Chem.* 2020;8:726.
65. Guan L, et al. ADMET-score—a comprehensive scoring function for evaluation of chemical drug-likeness. *Medchemcomm.* 2019;10(1):148–57.
66. Xu W, Ling P, Zhang T. Polymeric micelles, a promising drug delivery system to enhance bioavailability of poorly water-soluble drugs. *J Drug Deliv.* 2013;2013:340315.

Publisher's Note

Springer Nature remains neutral with regard to jurisdictional claims in published maps and institutional affiliations.